arXiv:1304.6516v1 [nucl-th] 24 Apr 2013

Charge form factors of two-neutron halo nuclei in halo EFT

P. Hagen,[1] H.-W. Hammer,[1] and L. Platter[2,3]
[1] *Helmholtz-Institut für Strahlen- und Kernphysik and Bethe Center for Theoretical Physics, Universität Bonn, 53115 Bonn, Germany*
[2] *Argonne National Laboratory, Physics Division, Argonne, IL 60439, USA*
[3] *Department of Fundamental Physics, Chalmers University of Technology, SE-412 96 Gothenburg, Sweden*

(Dated: April 23, 2013)

Abstract

We set up a formalism to calculate the charge form factors of two-neutron halo nuclei with S-wave neutron-core interactions in the framework of the halo effective field theory. The method is applied to some known and suspected halo nuclei. In particular, we calculate the form factors and charge radii relative to the core to leading order in the halo EFT and compare to experiments where they are available. Moreover, we investigate the general dependence of the charge radius on the core mass and the one- and two-neutron separation energies.

Keywords: halo nuclei, effective field theory, form factors, charge radii

I. INTRODUCTION

The determination of properties of nuclei along the neutron drip line poses one of the major challenges for modern nuclear experiment and theory. The associated observables are an important input to studies of stellar evolution and the formation of elements and provide insight into fundamental aspects of nuclear structure. Since these systems are weakly-bound, drip-line nuclei display novel phenomena associated with newly emerging degrees of freedom or, phrased differently, strong correlations.

Halo nuclei are one example where the transition to new degrees of freedoms becomes especially apparent. These nuclei have a tightly bound core with weakly-attached valence nucleons [1–4]. Usually, they are identified by an extremely large matter radius or a sudden decrease in the one- or two-nucleon separation energy along an isotope chain. Thus they display a separation of scales which exhibits itself also in low-energy scattering observables through a scattering length a that is large compared to the range of the nucleon-nucleus interaction R. Halo nuclei can be studied with an effective field theory (EFT) that exploits this separation of scales as a small expansion parameter R/a and is formulated in the relevant degrees of freedom [5, 6] (See, e.g., Refs. [7, 8] for recent reviews.) In this EFT, the core and the spectator particles are treated as the fundamental fields in the problem and the overall computational complexity decreases significantly. In contrast to ab initio approaches which try to predict nuclear observables from a fundamental nucleon-nucleon interaction, halo EFT essentially provides relations between different nuclear low-energy observables. On the one hand, it thus provides a framework that facilitates a consistent calculation of continuum and bound state properties when information on the nucleon-nucleus interaction is known. On the other hand, halo EFT can be used to determine two-body scattering properties from few-body observables if a sufficient number of them is known.

In a previous work, Canham and Hammer [9, 10] explored the universal properties and structure of $2n$ halo nuclei to next-to-leading order (NLO) in the expansion in $R/|a|$ by describing the halo nuclei as an effective three-body system consisting of a core and two loosely bound valence neutrons. Their main focus was the possibility of such three-body systems to display the universal Efimov effect [11] and on the structure of the halo candidates. In particular, the matter density form factors and mean square radii were calculated. Using this framework, Acharya et al. recently carried out a detailed analysis of the implications of a matter-radius measurement for the binding energy and existence of excited Efimov states in ^{22}C [12]. (For a selection of previous studies of the possibility of the Efimov effect in halo nuclei using three-body models, see Refs. [13–16].)

Halo EFT has also been extended to include Coulomb effects [17] and electromagnetic currents [18–21] in two-body halo nuclei. In this paper, we extend these studies to three-body halo nuclei. We consider the electromagnetic charge form factor and charge radius of two-neutron halo nuclei interacting through resonant S-wave interactions. While these quantities have not been measured yet for current S-wave halo candidates, we anticipate that the charge radius will be accessible in the near future due to the constant experimental progress in laser spectroscopy techniques on radioactive ions that facilitate a measurement of the atomic isotope shift.

This manuscript is organized out as follows: In Secs. II, III and IV, we lay out the field theoretical formalism required for the calculation of strong interaction observables in two- and three-body S-wave halos. The trimer Greens functions are introduced in Sec. V and the calculation of the charge form factor is discussed in Sec. VI. Our results for the form factors and radii including error estimates are presented in Sec. VII. Finally, we conclude in Sec. VIII. Detailed expressions for the various contributions to the form factor are given in the Appendix.

II. EFFECTIVE LANGRANGIAN

We set up a non-relativistic effective field theory for a core (c) with spin 0, mass m_0 and electromagnetic charge $\mathcal{Z}e$, interacting with two neutrons (n) with spin 1/2 and mass m_1. The core is described by a scalar field ψ_0 and the neutrons are described by a two-component spinor field $\vec{\psi}_1 = \binom{n_\uparrow}{n_\downarrow}$.

We assume that all two-particle interactions are short-ranged and dominated by S-wave resonances. The treatment of resonant P- and higher partial wave interactions will be left for future work. If they are non-resonant, higher-partial wave interactions are suppressed by three powers of R/a [5, 6]. The core-neutron interaction is described by a spin-1/2 dimer field $\vec{d}_1 = \begin{pmatrix} d_{1,\uparrow} \\ d_{1,\downarrow} \end{pmatrix}$ and the interaction of the two neutrons is described by a spin-0 dimer-field d_0. The labeling and indices are chosen to simplify the notation for the three-body equations derived below. Moreover, we allow for a three-body contact interaction between the core and the two neutrons which is described by a spin-0 trimer auxiliary field t. Note, that our choice to introduce auxiliary fields does not imply bound states in the corresponding channels and merely is a convenient way to introduce interactions.

In addition to the strong interactions between the neutrons and the core, we include electromagnetic interactions with a vector potential A_μ. The interaction terms are obtained by minimal coupling which insures gauge invariance: $i\partial_\mu \mapsto i\partial_\mu - \hat{Q}A_\mu$, where $\hat{Q}$ is the charge operator. In our case only the core has non-vanishing charge $\mathcal{Z}e$, such that $\hat{Q}\psi_0 = \mathcal{Z}e\,\psi_0$ and $\hat{Q}\vec{\psi}_1 = 0$ holds. For convenience, we choose Coulomb gauge where $(\vec{\nabla}\cdot\vec{A}) = 0$. Since we restrict our analysis to leading order (LO), non-minimal coupling terms do not contribute. The effective Lagrangian can then be written as the sum of one-, two- and three-body contributions, $\mathcal{L} = \mathcal{L}^{(1)} + \mathcal{L}^{(2)} + \mathcal{L}^{(3)}$, where

$$\begin{aligned}
\mathcal{L}^{(1)} &= \psi_0^\dagger\left(i\partial_0 + \frac{\vec{\nabla}^2}{2m_0}\right)\psi_0 \;+\; \vec{\psi}_1^\dagger\left(i\partial_0 + \frac{\vec{\nabla}^2}{2m_1}\right)\vec{\psi}_1 \;-\; \mathcal{Z}e\;\psi_0^\dagger A_0\,\psi_0 \\
&\quad - \frac{1}{2m_0}\psi_0^\dagger\left(i2\hat{Q}\vec{A}\cdot\vec{\nabla} + \hat{Q}^2\vec{A}^2\right)\psi_0\ , \\
\mathcal{L}^{(2)} &= \Delta_1\,\vec{d}_1^\dagger\vec{d}_1 \;-\; g_1\left[\vec{d}_1^\dagger\vec{\psi}_1\,\psi_0 + \psi_0^\dagger\,\vec{\psi}_1^\dagger\vec{d}_1\right] \\
&\quad + \;\Delta_0\,d_0^\dagger d_0 \;-\; \frac{g_0}{2}\left[d_0^\dagger\,(\vec{\psi}_1^{\,\mathrm{T}}P\,\vec{\psi}_1) + (\vec{\psi}_1^{\,\mathrm{T}}P\,\vec{\psi}_1)^\dagger\,d_0\right]\ , \\
\mathcal{L}^{(3)} &= \Omega\,t^\dagger\,t \;-\; h\left[t^\dagger\,\psi_0\,d_0 + (\psi_0\,d_0)^\dagger t\right]\ .
\end{aligned} \tag{1}$$

Because we focus on resonant S-wave interactions, the electromagnetic interaction appears only in $\mathcal{L}^{(1)}$.

The two-body part $\mathcal{L}^{(2)}$ includes the bare dimer propagators and the coupling of a dimer to two single particles. The bare parameters Δ_0, g_0, Δ_1 and g_1 depend on the ultraviolet cutoff Λ. At LO the parameters Δ_i and g_i ($i = 1, 2$) are not independent. Physical observables only depend on the the combination g_i^2/Δ_i. The spin projection matrix P projects the two neutrons on the spin-singlet. Its components are the corresponding Clebsch-Gordon coefficients, leading to

$$P \;=\; \frac{1}{\sqrt{2}} \left(\begin{smallmatrix} 0 & 1 \\ -1 & 0 \end{smallmatrix} \right) \;=\; -P^\dagger \;, \tag{2}$$

such that $PP^\dagger \;=\; \mathbb{1}_2/2$ and $\mathrm{Tr}[PP^\dagger] \;=\; 1$.

Finally, $\mathcal{L}^{(3)}$ represents the three-body interaction written in terms of a trimer auxilliary field [22]. It includes the bare trimer propagator and the coupling of the trimer t to the d_0-dimer and the core field ψ_0. Writing the three-body interaction using a trimer auxilliary field will be convenient for deriving the form factor expressions below. The bare parameters Ω and h depend on the ultraviolet cutoff Λ. Again only the combination h^2/Ω contributes to observables at LO.

There exists a whole class of equivalent theories in the three particle sector. Integrating out the auxiliary fields, one can show that different choices of $\mathcal{L}^{(2)}$ and $\mathcal{L}^{(3)}$ can be transformed into the same theory without dimer and trimer fields up to four- and higher-body interactions. To demonstrate this, we eliminate the trimer field t using the classical equation of motion, resulting in

$$\mathcal{L}^{(3)} \;\mapsto\; -H_0(\psi_0 d_0)^\dagger(\psi_0 d_0) \;, \tag{3}$$

where $H_0 \;=\; \frac{h^2}{\Omega}$. Repeating this step for the dimer fields $\vec{d}_1$ and d_0 then yields

$$\begin{aligned} \mathcal{L}^{(2)} \;&\mapsto -\, C_0^1(\psi_0\vec{\psi}_1)^\dagger(\psi_0\vec{\psi}_1) - C_0^0(\vec{\psi}_1^{\,\mathrm{T}} P\,\vec{\psi}_1)^\dagger(\vec{\psi}_1^{\,\mathrm{T}} P\vec{\psi}_1) \;, \\ \mathcal{L}^{(3)} \;&\mapsto -\, H_0' \left(\psi_0\,(\vec{\psi}_1^{\,\mathrm{T}} P\vec{\psi}_1)\right)^\dagger \left(\psi_0\,(\vec{\psi}_1^{\,\mathrm{T}} P\vec{\psi}_1)\right) \;+\; \mathcal{L}^{(\geq 4)} \;, \end{aligned} \tag{4}$$

where $C_0^1 \;=\; \frac{g_1^2}{\Delta_1}$, $C_0^0 \;=\; \frac{g_0^2}{4\Delta_0}$, and $H_0' \;=\; \frac{C_0^0 H_0}{\Delta_0}$. The term $\mathcal{L}^{(\geq 4)}$ includes interactions of four or more particles. In this work, we will only consider processes with at most three particles and therefore neglect $\mathcal{L}^{(\geq 4)}$. By this procedure, physical observables will be unchanged as long as the coupling constants are chosen appropriately. In particular, the trimer field could also have been introduced in another channel, such as

$$\tilde{\mathcal{L}}^{(3)} = \Omega\, t^\dagger\, t \;-\; h \left[t^\dagger\,(\vec{\psi}_1^{\,\mathrm{T}} P\vec{d}_1) + (\vec{\psi}_1^{\,\mathrm{T}} P\vec{d}_1)^\dagger t \right] \;, \tag{5}$$

without changing any three-body observables.

In order to write down the derived expressions more compactly, we define the mass parameters:

$$M_{\mathrm{tot}} = m_0 + 2m_1 \;, \qquad M_i = M_{\mathrm{tot}} - m_i \;, \qquad \mu_i = \frac{m_0 m_1^2}{m_i M_i} \;, \qquad \tilde{\mu}_i = \frac{m_i M_i}{M_{\mathrm{tot}}} \;. \tag{6}$$

In the following, we use Feynman rules in momentum space to calculate the properties of the *cn*, *nn*, and *cnn* systems. In the Feynman diagrams, particles, dimers and trimers are denoted by single, double and triple lines, respectively. In addition, propagators are represented by arrows, photon couplings by rectangles and all other couplings by ellipses. These symbols are empty if they correspond to bare and filled if they correspond to full, interacting quantities. Since we consider a non-relativistic theory, the one-body properties are not modified by interactions. We thus start with the two-body problem in the next section.

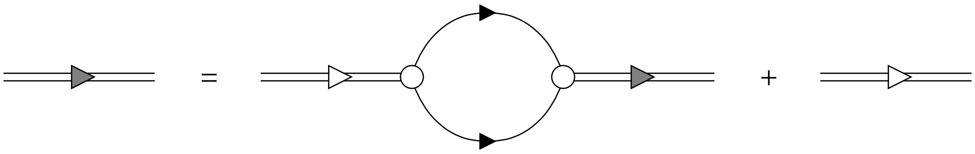

FIG. 1: Diagrammatic representation of the integral equation for the full dimer propagator. Particles and dimers are denoted by single and double lines, respectively. The bare (full) dimer propagators are indicated by the empty (filled) arrow.

III. TWO-BODY PROBLEM

We start by calculating the full dimer propagator $D_i(p_0, \mathbf{p})$ with three-momentum $\mathbf{p}$ and energy p_0 for the dimer field with index $i = 0, 1$, corresponding to the nn and cn channels, respectively. The integral equation is depicted in Fig. 1 in terms of Feynman diagrams. Using the Feynman rules derived from the effective Lagrangian (1), we find

$$\begin{aligned} iD_i(p_0,\mathbf{p}) \ &= \frac{i}{\Delta_i}\ \left(-i\Sigma_i(p_0,\mathbf{p})\right)\ iD_i(p_0,\mathbf{p}) \ + \ \frac{i}{\Delta_i} \ = \ i\left[\Delta_i - \Sigma_i(p_0,\mathbf{p})\right]^{-1} \ , \\ -i\Sigma_i(p_0,\mathbf{p}) \ &= i\frac{s_i\, g_i^2 \mu_i}{\pi^2}\left[\Lambda - \frac{\pi}{2}\sqrt{2\mu_i\left(\frac{\mathbf{p}^2}{2M_i} - p_0 - i\varepsilon\right)}\right] \ , \end{aligned} \tag{7}$$

where $s_i = \delta_{i0}/2 + \delta_{i1}$ is a symmetry factor and $-i\Sigma_i(p_0, \mathbf{p})$ is the dimer self energy. It is linearly divergent and has to be regularized. For this purpose, we choose a momentum cutoff Λ which is the same in both channels.

Matching the two-body T-matrix obtained from the propagator (7) for $\mathbf{p} = 0$ and $p_0 = k^2/(2\mu_i)$ to the effective range expansion of the S-wave scattering amplitude

$$f_i(k) \ = \ \left[-\frac{1}{a_i} + \mathcal{O}(k^2) - ik\right]^{-1} \tag{8}$$

with scattering length a_i, we eliminate the dependence on the cutoff Λ. This leads to the renormalization condition for the two-particle couplings

$$\frac{1}{a_i} \ = \ \frac{2\pi\Delta_i}{s_i\, g_i^2\mu_i} + \frac{2}{\pi}\Lambda \tag{9}$$

and the renormalized, full dimer propagator

$$D_i(p_0,\mathbf{p}) \ = \ \frac{2\pi}{s_i\, g_i^2\mu_i}\ \left[\frac{1}{a_i} - \sqrt{2\mu_i\left(\frac{\mathbf{p}^2}{2M_i} - p_0 - i\varepsilon\right)}\right]^{-1} \ . \tag{10}$$

For positive scattering length a_i, this propagator has one pole on the first Riemann sheet of the complex square root with the positive residue

$$Z_i \ = \ \frac{2\pi}{s_i\, g_i^2\mu_i^2}\,\frac{1}{a_i}\ . \tag{11}$$

This pole corresponds to a two-body bound state with binding energy $B_i = 1/(2\mu_i a_i^2)$. For negative a_i there is a pole with negative residue on the unphysical, second Riemann sheet.

The leading correction to the propagator (10) is due to the effective range. It could be included by making the dimer fields dynamical as discussed, e.g., in Refs. [23–25]. Here, we stay at leading order in the EFT expansion and neglect effective range corrections.

IV. THREE-BODY PROBLEM

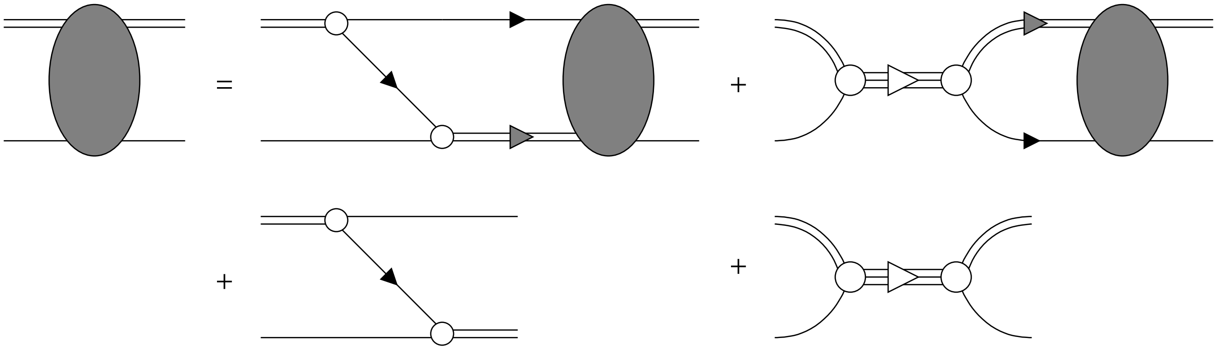

FIG. 2: Diagrammatic representation of the integral equation for the particle-dimer T-matrix. Particles, dimers, and trimers are denoted by single, double, and triple lines, respectively. The bare (full) propagators are indicated by the empty (filled) arrows.

We proceed by calculating the T-matrix element T_{ij} for the scattering process of a dimer and a particle. The dimer and particle in the incoming (outgoing) channel are both labeled by the index i (j), respectively. We focus on the dimer-particle T-matrix as a central quantity, since all other three-body observables can be obtained from it. The integral equation for the T-matrix is depicted in Fig. 2 in terms of Feynman diagrams. The matrix structure of the equation is implicit in Fig. 2.

The derivation of the corresponding expressions can be performed in several steps. First, we project in- and outgoing states onto the spin-singlet using the projection operator from Eq. (2). External dimer fields are then renormalized with the wave function renormalization factors from Eq. (11) via

$$T_{ij} \;\mapsto\; |Z_i|^{\frac{1}{2}}\, T_{ij}\, |Z_j|^{\frac{1}{2}} \quad . \tag{12}$$

The absolute values in Eq. (12) are only required for $i, j = 0$ because $Z_0 < 0$. This channel corresponds to a neutron-neutron dimer which is unbound and requires no wave function renormalization factor. In this case, Eq. (12) simply provides a convenient redefinition of the amplitude but has no physical significance.

We work in the center-of-mass frame, in which the on-shell T-matrix only depends on the total energy E and the relative momenta in the ingoing and outgoing channels $\mathbf{p}$ and $\mathbf{k}$, respectively. If the dimer and the particle have ingoing (outgoing) three-momenta $\mathbf{p}_1$ and $\mathbf{p}_2$ ($\mathbf{k}_1$ and $\mathbf{k}_2$) in a general frame, the relative momenta are

$$\mathbf{p} \;=\; \frac{m_i}{M_{\text{tot}}}\mathbf{p}_1 - \frac{M_i}{M_{\text{tot}}}\mathbf{p}_2 \;, \qquad \mathbf{k} \;=\; \frac{m_j}{M_{\text{tot}}}\mathbf{k}_1 - \frac{M_j}{M_{\text{tot}}}\mathbf{k}_2 \;. \tag{13}$$

The T-matrix can be decomposed into partial wave contributions $T^{[\ell m,\ell' m']}$. The Wigner-Eckart theorem then implies that T is diagonal in ℓ and m and can be written as $T^{[\ell m,\ell' m']} = \delta_{\ell\ell'}\delta_{mm'}T^{[\ell]}$. The resulting 2×2-matrix integral equation for angular momentum ℓ is a generalization of the Skorniakov-Ter-Martyrosian (STM) equation [26] and reads

$$T^{[\ell]}(E,p,k) \;=\; \int_0^\Lambda \mathrm{d}q \; R^{[\ell]}(E,p,q)\; \bar{D}(E,q)\; T^{[\ell]}(E,q,k) \;+\; R^{[\ell]}(E,p,k) \;, \tag{14}$$

where Λ is an ultraviolet cutoff on the loop-momentum in the three-particle sector. The components of the interaction matrix $R^{[\ell]}$ are given through

$$\begin{aligned} R^{[\ell]}_{ij}(E,p,k) \ &= \ \frac{(1-\delta_{i0}\delta_{j0})}{\sqrt{s_i s_j}}\,(-1)^\ell\,\frac{2\pi}{\sqrt{|a_i||a_j|}}\,\frac{M_{\mathrm{tot}}-m_i-m_j}{\mu_i\mu_j}\,\frac{1}{pk}\,Q_\ell\big(c_{ij}(E,p,k)\big) \\ &\quad - \delta_{i0}\delta_{j0}\,\delta_{\ell 0}\ H\ , \\ c_{ij}(E,p,k) \ &= \ \frac{M_{\mathrm{tot}}-m_i-m_j}{pk}\left(\frac{p^2}{2\mu_j}+\frac{k^2}{2\mu_i}-E-i\varepsilon\right)\ , \end{aligned} \tag{15}$$

where Q_ℓ are the analytically continued Legendre functions of the second kind. In our numerical calculations, we will only need

$$Q_0(c) \ = \ \begin{cases} \operatorname{arctanh}(1/c) & : |c|>1\ , \\ \operatorname{arctanh}(c)+i\frac{\pi}{2} & : |c|<1\ . \end{cases} \tag{16}$$

The form of Q_0 is determined by taking the limit $\varepsilon \to 0^+$ in the integral equation. Moreover, $H = |Z_0|h^2/\Omega$ is the redefined three-body coupling, which depends on the cutoff Λ. It only contributes for angular momentum $\ell = 0$. The dimer matrix is diagonal in the channel indices: $\bar{D} = \mathrm{diag}(\bar{D}_0, \bar{D}_1)$ with

$$\bar{D}_i(E,q) \ = \ \frac{\mu_i|a_i|}{2\pi^2}\,\frac{q^2}{-\frac{1}{a_i}+\sqrt{b_i(E,q)}}\ , \qquad b_i(E,q) \ = \ 2\mu_i\left(\frac{q^2}{2\tilde{\mu}_i}-E-i\varepsilon\right)\ . \tag{17}$$

Note that an overall factor $-q^2/(2\pi^2|Z_i|)$ from the measure of the integration over the loop momentum q and the dimer wave function renormalization has been absorbed in $\bar{D}_i$ for notational convenience.

Assuming the existence of an S-wave three-body bound state at energy $E = -B$, the transition amplitude can be decomposed as

$$T^{[\ell]}(E,p,k) \ = \ -\delta_{\ell 0}\frac{\vec{\mathcal{B}}(p)\cdot\vec{\mathcal{B}}^\dagger(k)}{E+B+i\varepsilon} \quad + \quad \text{regular terms}\ . \tag{18}$$

The residue of the bound state pole factors into wave functions $\vec{\mathcal{B}}(p)$ depending only on one single momentum, and the remaining part is a regular function in the energy. Inserting Eq. (18) into Eq. (14) yields the bound state equation

$$\vec{\mathcal{B}}(p) \ = \ \int_0^\Lambda \mathrm{d}q\ R^{[0]}(E,p,q)\ \bar{D}(E,q)\ \vec{\mathcal{B}}(q)\ . \tag{19}$$

This generalized eigenvalue problem has an Efimov-like spectrum of three-body bound state energies. For a given cutoff Λ, we then fix the unknown three-body parameter H such that Eq. (19) has a solution at the desired value $E = -B$. In this way, the three-body coupling is renormalized and other three-body observables can be predicted. In particular, Eq. (14) can be solved numerically in order to determine the T-matrix for three-body scattering observables.

In the following, we will consider only three-body observables in the S-wave ($\ell = 0$) channel and drop the index "[0]" on the quantities $R^{[0]}$ and $T^{[0]}$ for notational simplicity.

From the T-matrix, we can derive the scattering amplitude and scattering length for dimer-particle scattering. Since the two-neutron system is not bound, only the element T_{11} of the 2×2 T-matrix in Eq. (14) describes a physical scattering process, namely the scattering of a neutron from a cn bound state:

$$T_{11}\left(\frac{p^2}{2\tilde{\mu}_1} - \frac{1}{2\mu_1 a_1^2},\ p,\ p\right) = \frac{2\pi}{\tilde{\mu}_1}\frac{1}{p\cot\delta_{cn-n}(p) - ip} \tag{20}$$

where the reduced masses μ_1 and $\tilde{\mu}_1$ are defined in Eq. (6).

V. TRIMER GREENS FUNCTIONS

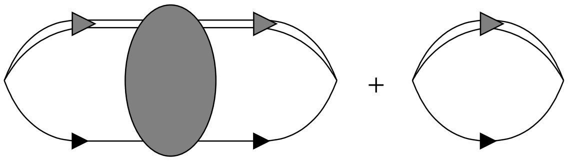

FIG. 3: Feynman diagrams contributing to the full trimer propagator t. Particles, dimers, and trimers are denoted by single, double, and triple lines, respectively. Otherwise the notation is as in Fig. 2.

In order to calculate the charge form factor of the three-body bound states corresponding to two-neutron halo nuclei, we need the trimer wave function renormalization Z_{tr} which is given by the residue of the bound state pole in the full trimer propagator including interactions. The Feynman diagrams contributing to the propagator are shown in Fig. 3. For a trimer at rest, it can be written as

$$t(E,0) = \int_0^\Lambda \mathrm{d}q \int_0^\Lambda \mathrm{d}q'\, \bar{D}_0(E,q)\, T_{00}(E,q,q')\, \bar{D}_0(E,q') \quad + \quad \text{regular terms}\ . \tag{21}$$

Because the three-body interaction from Eq. (1) acts only in the $i = 0$ channel, only T_{00} contributes in Eq. (21). The trimer wave function renormalization can be extracted from the relation

$$Z_{\text{tr}} = -\lim_{E\to -B}(E+B)\, t(E,0)\ . \tag{22}$$

The trimer self energy is given by all trimer-irreducible contributions to the propagator and can be defined as

$$\Sigma(E) = t(E,0)\big|_{H=0}\ , \tag{23}$$

where the three-body force is set to zero in the evaluation of T_{00}. Using $\Sigma(E)$, the trimer propagator can also be written as

$$t(E,0) = \frac{\Sigma(E)}{1 - H\,\Sigma(E)}\ . \tag{24}$$

Requiring that $t(E,0)$ has a bound state pole at $E = -B$, Eq. (24) directly leads to the relation

$$\Sigma(-B) = 1/H\ . \tag{25}$$

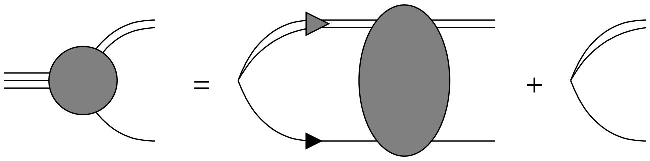

FIG. 4: Diagrammatic representation of the irreducible trimer-dimer-particle three-point function $\mathcal{G}^{\rm irr}$. The three-body force H is set to zero in the evaluation of the particle-dimer T-matrix. Notation is as in Fig. 3.

In the explicit expressions for the trimer form factor (cf. Appendix A), we need the irreducible trimer-dimer-particle three-point function defined by

$$\mathcal{G}_i^{\rm irr}(E,p) \ := \int_0^\Lambda {\rm d}q\, \bar{D}_0(E,q)\ T_{0i}(E,q,p)\Big|_{H=0} \ + \ \delta_{0i}\ , \tag{26}$$

where again trimer-reducible contributions are removed by setting $H = 0$ in the integral equation for T_{0i}. The corresponding Feynman diagrams are depicted in Fig. 4. Inserting Eq. (14) into Eq. (26) and writing $\vec{\mathcal{G}}^{\rm irr} = \begin{pmatrix} \mathcal{G}_0^{\rm irr} \\ \mathcal{G}_1^{\rm irr} \end{pmatrix}$, yields a matrix integral equation for the irreducible trimer-dimer-particle three-point function

$$\vec{\mathcal{G}}^{\rm irr}(E,p) \ = \ \int_0^\Lambda {\rm d}q\, R(E,p,q)\Big|_{H=0} \bar{D}(E,q)\, \vec{\mathcal{G}}^{\rm irr}(E,q) \ + \ \vec{e_0}\ , \tag{27}$$

where $(\vec{e_0})_i = \delta_{0i}$. $\vec{\mathcal{G}}^{\rm irr}$ depends on the cutoff Λ, but the combination $\sqrt{Z_{\rm tr}}\, H\, \vec{\mathcal{G}}^{\rm irr}$ is independent of Λ up to an overall sign. This is exactly the combination that enters into the form factor calculation.

VI. CHARGE FORMFACTORS

We are now in a position to calculate the charge formfactor $\mathcal{F}_{\rm E}$ of a cnn halo system with resonant S-wave interactions. The form factor can be extracted from the matrix element of the electromagnetic current j_μ between trimer states. We will denote the in- and outgoing three-momenta of the trimer by $\mathbf{P}$ and $\mathbf{K}$, respectively. It is convenient to extract the charge form factor from the matrix element of the zeroth component of the electromagnetic current

$$\langle\, t(K_0, \mathbf{K})\,|\, j_0\,|\, t(P_0, \mathbf{P})\,\rangle \ = \ (-ie\mathcal{Z})\ \mathcal{F}_{\rm E}(\mathbf{Q}^2) \tag{28}$$

in the Breit frame, where no energy is transferred by the photon, i.e. $P_0 = K_0$ and $\mathbf{P}^2 = \mathbf{K}^2$. The charge formfactor in Eq. (28), then depends only on the three-momentum transfer $\mathbf{Q}^2 = (\mathbf{K} - \mathbf{P})^2$.

The LSZ reduction formula implies that the current matrix element in Eq. (28) can be expressed as [27]

$$\begin{aligned} \langle\, t(K_0, \mathbf{K})\,|\, j_0\,|\, t(P_0, \mathbf{P})\,\rangle \ &= \sqrt{Z_{\rm tr}}\, \Sigma(-B)^{-1}\ i\Gamma_0(\mathbf{Q})\ \Sigma(-B)^{-1} \sqrt{Z_{\rm tr}} \\ &= Z_{\rm tr}\, H^2\ i\Gamma_0(\mathbf{Q})\ , \end{aligned} \tag{29}$$

where $i\Gamma_0(\mathbf{Q})$ is the sum of all irreducible Feynman diagrams with external trimer lines and a photon coupled to the core.

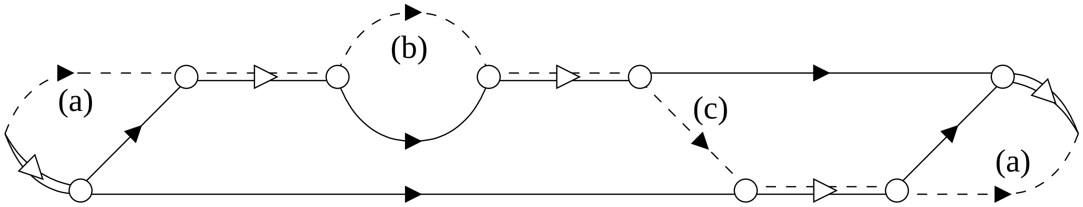

FIG. 5: Exemplary irreducible graph contributing to the trimer form factor. The dashed line represents the core field which either (a) propagates parallel to the d_0-dimer, (b) appears within a d_1-dimer loop or (c) is exchanged between d_1-dimers. Otherwise the notation is as in Fig. 4.

In order to motivate the different contributions to $i\Gamma_0(\mathbf{Q})$, we consider the typical irreducible graph shown in Fig. 5. The photon can only couple to the core field c indicated by dashed lines, but for the moment we suppress the photon-core coupling.[1] Within such a diagram, the core (a) propagates either parallel to the d_0-dimer, (b) appears within a d_1-dimer loop, or (c) is exchanged between between two d_1-dimers. In fact, these are the only 3 possibilities for a single core propagator to appear in an arbitrary irreducible trimer graph. Thus, including the photon-core coupling and summing over all such diagrams the form factor derived from the transition amplitude through Eq. (28) and Eq. (29), can be written as the sum of three contributions

$$\mathcal{F}_{\mathrm{E}} = \mathcal{F}_{\mathrm{E}}^{(a)} + \mathcal{F}_{\mathrm{E}}^{(b)} + \mathcal{F}_{\mathrm{E}}^{(c)} , \tag{30}$$

corresponding to the cases (a), (b), and (c). In all three contributions the irreducible trimer-dimer-particle three-point function $\vec{\mathcal{G}}^{\mathrm{irr}}$ from Eq. (26) appears naturally.

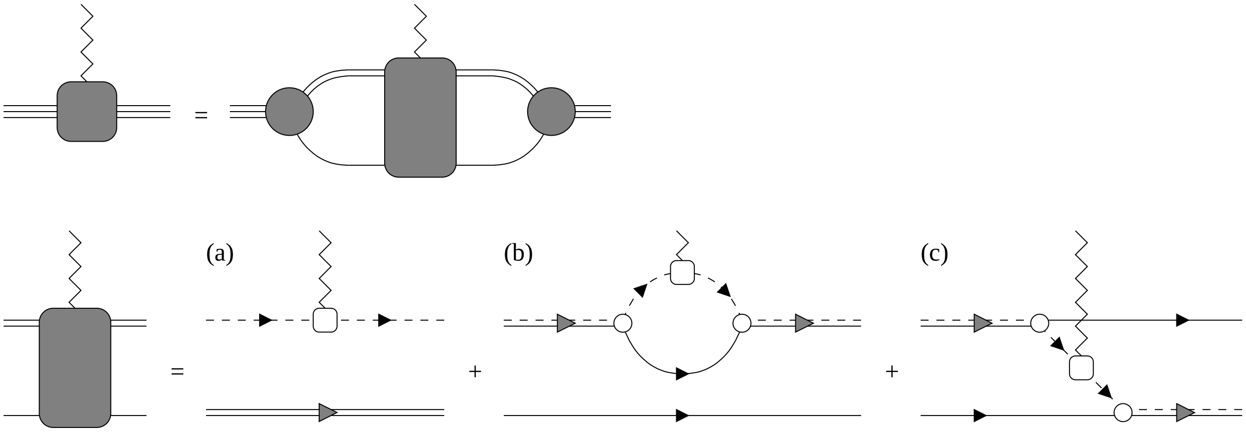

FIG. 6: Diagrammatical representation of the form factor matrix element (28). The contributions fall into three different classes (a), (b), and (c). Notation is as in Fig. 4.

In Fig. 6, the decomposition of the form factor matrix element (28) into the three classes of diagrams is illustrated pictorially. The filled circle represents $\vec{\mathcal{G}}^{\mathrm{irr}}$ from Eq. (26). Performing shifts in the loop momenta of order $Q = |\mathbf{Q}| \ll \Lambda$ one can express $\mathcal{F}_{\mathrm{E}}^{(a)}$, $\mathcal{F}_{\mathrm{E}}^{(b)}$, and $\mathcal{F}_{\mathrm{E}}^{(c)}$

---

[1] Of course the d_1-dimer also carries charge, but the photon coupling to d_1 appears only at next-to-leading order where the dimers are dynamical.

through integrals symmetric in the momenta. The various contributions are derived in Appendix A and explicit expressions are given in Eqs. (A3), (A6) and (A8), respectively.

At $Q^2 = 0$, the charge formfactor is normalized to one. This normalization is automatically reproduced in our formalism. For small momentum transfer, the form factor can be expanded in powers of Q^2 as:

$$\mathcal{F}_{\mathrm{E}}(Q^2) \;=\; 1 - \frac{\langle r_{\mathrm{E}}^2 \rangle}{6} Q^2 \;+\; \mathcal{O}(Q^4) \;, \tag{31}$$

where $\langle r_{\mathrm{E}}^2 \rangle$ is the charge radius.

In practice, we calculate the form factors for finite momentum transfer and extract the the charge radius $\langle r_{\mathrm{E}}^2 \rangle$ by numerically taking the limit

$$\langle r_{\mathrm{E}}^2 \rangle \;=-6 \lim_{Q^2 \to 0^+} \frac{d\mathcal{F}_{\mathrm{E}}}{dQ^2} \;. \tag{32}$$

Here, we have to keep in mind, that in our effective theory the core and the neutrons are treated as pointlike. Their size enters only in counter terms that appear at higher orders. In typical halo nuclei, however, the charge radius of the core can not be neglected. In this work, we thus interpret the calculated radius as the charge radius of the *cnn* halo nucleus relative to the charge radius of the core. The small negative charge radius of the neutron $\langle r_{\mathrm{E}}^2 \rangle_n = -0.115(4)$ fm^2 [28] is neglected. In order to get the full charge radius of the *cnn* halo nucleus $\langle r_{\mathrm{E}}^2 \rangle_{cnn}$, we therefore have to quadratically add our result to the charge radius of the core $\langle r_{\mathrm{E}}^2 \rangle_c$:

$$\langle r_{\mathrm{E}}^2 \rangle_{cnn} \;=\; \langle r_{\mathrm{E}}^2 \rangle_c \;+\; \langle r_{\mathrm{E}}^2 \rangle \;, \tag{33}$$

or simply quote the difference $\delta \langle r_{\mathrm{E}}^2 \rangle \;:=\; \langle r_{\mathrm{E}}^2 \rangle_{cnn} - \langle r_{\mathrm{E}}^2 \rangle_c$. This prescription follows directly if the total charge distribution is a convolution of the charge distributions of the halo and the core. The differences of nuclear charge radii $\delta \langle r_{\mathrm{E}}^2 \rangle$ were measured for a whole range of isotopes, see e.g. [29–33]. In the next section, we will compare these results with our theory where it is applicable.

VII. RESULTS

We now apply our effective field theory to concrete physical systems. Our theory applies directly to two-neutron halo nuclei with $J^\pi = 0^+$ and with a $J^\pi = 0^+$ core. Assuming that the spin of the core is inert due to the large mass of the core compared to the neutrons, we can also consider more general systems with quantum numbers J^π, $(J \pm 1/2)^\pi$, and J^π of the *c*-, *cn*-, and *cnn*-systems, respectively. From now on, we write m_n for the neutron mass and m_c for the core mass for convenience.

In order to have a bound or virtual *cn*-dimer and a bound *cnn*-trimer their one- and two-neutron separation energies $B_{cn} \equiv B_1$ and $B_{cnn} \equiv B$ have to obey $B_{cnn} > \max(B_{cn}, 0)$. Moreover, we denote the first excitation energy of the core by E_c^* and the one-neutron separation energy by B_{c-n}. As discussed in the introduction, the expansion parameter of our theory $R_{\mathrm{core}}/R_{\mathrm{halo}}$ is roughly R/a. In order to obtain better estimates, we compare the typical energy scales E_{halo} and E_{core} of the neutron halo and the core, respectively. To estimate E_{halo}, we choose the one- or two-neutron separation energy B_{cn} or B_{cnn}. The energy scale of the core is estimated by its excitation energy E_c^* or its one-neutron separation energy B_{c-n}. The square root of the energy ratio $R_{\rm core}/R_{\rm halo} \approx \sqrt{|E_{\rm halo}/E_{\rm core}|}$ then yields an estimate for the expansion parameter of the effective theory. For our error estimates, we take the largest value for $R_{\rm core}/R_{\rm halo}$ that can be obtained this way.

We fix the values of all quantum numbers J^π, masses, and energies by taking data from the National Nuclear Data Center (NNDC) [35]. The cn-scattering length is determined from the relation $a_1 \equiv a_{cn} = \text{sign}(B_1)/\sqrt{2\mu_1|B_1|}$. Thus cn-states with negative B_1 are treated as virtual two-body states with negative scattering length a_1. This approximation corresponds to neglecting the imaginary part of the binding momentum for resonances. For the nn-scattering length, we take the value $a_0 \equiv a_{nn} = -18.7(6)$ fm from Gonzales Trotter et al. [34].

The lightest isotopes for which there is either experimental evidence for their $2n$-halo nature or which are good candidates for such a system, are ^{6}He, ^{11}Li, ^{14}Be, ^{17}B and ^{22}C. Since the J^π-quantum numbers of ^{6}He and ^{17}B indicate that P-wave contributions must be dominant, we apply our effective theory to ^{11}Li, ^{14}Be and ^{22}C.

In Tab. I, we summarize the effective theory parameters and our predictions for the charge radii relative to the core in ^{11}Li, ^{14}Be and ^{22}C. Uncertainties in the energies are only quoted if they are larger than 1%. The small uncertainties in the nuclear masses can be neglected. For ^{11}Li and ^{14}Be, the expansion parameter $R_{\rm core}/R_{\rm halo}$ is typically not much smaller than 1. As a consequence, the main uncertainty in our calculation for these systems is from the next-to-leading order corrections in the effective theory. In the ^{22}C halo nucleus, the main uncertainty is from the poor knowledge of the binding energies. Below, we discuss our analysis for each halo nucleus in detail.

c	J^π_c	m_c [MeV]	E^*_c [MeV]	B_{c-n} [MeV]	$\delta\left\langle r_{\rm E}^2\right\rangle$ [fm^2]
cn	J^π_{cn}	B_{cn} [MeV]	$\frac{B_{cn}}{E^*_c}$	$\frac{B_{cn}}{B_{c-n}}$	$\delta\left\langle r_{\rm E}^2\right\rangle_{\rm exp}$ [fm^2]
cnn	J^π_{cnn}	B_{cnn} [MeV]	$\frac{B_{cnn}}{E^*_c}$	$\frac{B_{cnn}}{B_{c-n}}$	
^{9}Li	$\frac{3}{2}^-$	8406	2.69	4.06	1.68(62)
^{10}Li	$(2^-, 1^-)$	$-0.026(13)$	-0.10^2	-0.08^2	1.171(120) [29]
^{11}Li	$\frac{3}{2}^-$	0.37	0.37^2	0.30^2	
^{12}Be	0^+	11201	2.10	3.17	0.41(32)
^{13}Be	$(\frac{1}{2}^-)$	$-0.51(1)$	-0.49^2	-0.40^2	$--$
^{14}Be	0^+	1.27(13)	0.78^2	0.63^2	
^{20}C	0^+	18664	$--$	2.9(3)	$1.66^{+\infty}_{-0.49}$
^{21}C	$\frac{1}{2}^+$	$-0.014(467)$	$--$	-0.07^2	$--$
^{22}C	0^+	0.11(6)	$--$	0.20^2	

TABLE I: Effective theory parameters, estimates of the expansion parameter, and predicted electric charge radii relative to the core $\delta\left\langle r_{\rm E}^2\right\rangle$ from Eq. (32) for the halo nuclei ^{11}Li, ^{14}Be and ^{22}C. Further explanations are given in the text.

The ^{11}Li halo nucleus and the ^{9}Li core have both the quantum numbers $J^\pi = \frac{3}{2}^-$ while ^{10}Li appears to have either $J^\pi = 2^-$ or 1^-. There is some evidence that both S- and P-wave components contribute to the neutron halo [2]. However, we will analyze ^{11}Li under the assumption that only the S-wave contributes in LO and test the consistency of our assumption with the data. P-wave contributions will enter in higher orders. The two-neutron separation energy of ^{11}Li is 0.37 MeV and ^{10}Li is 26(13) keV above the n-^{9}Li

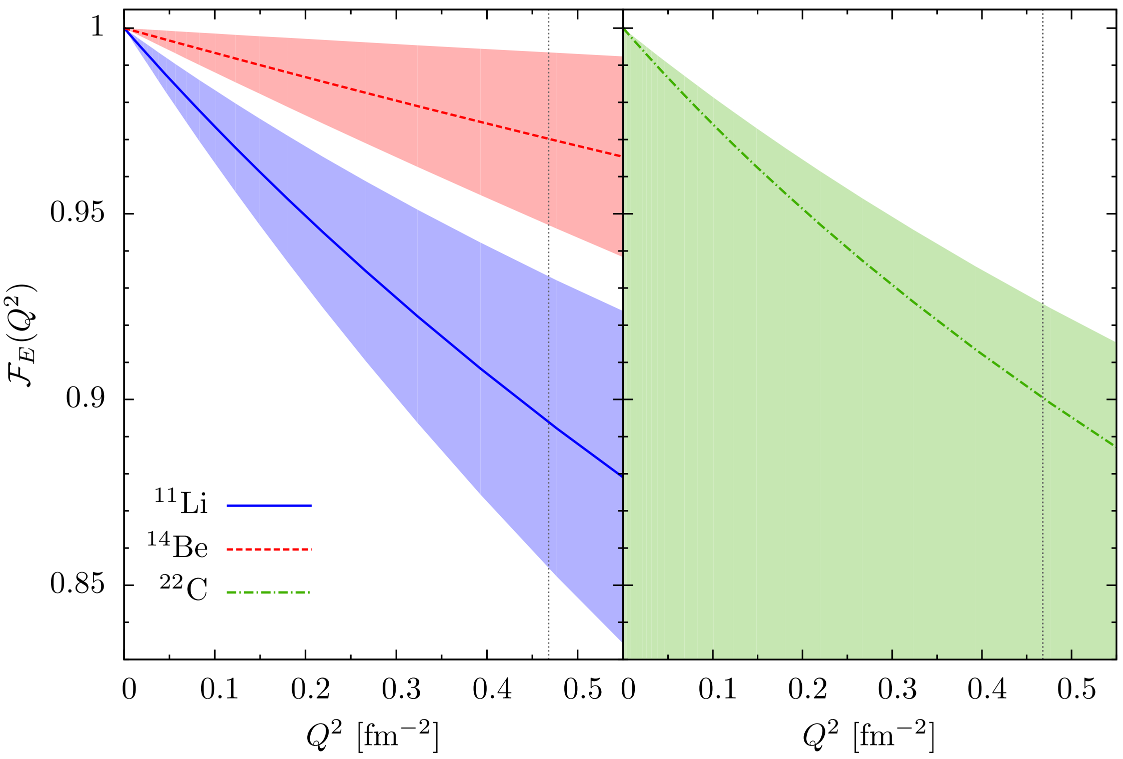

FIG. 7: (Color online) The charge form factor $\mathcal{F}_{\mathrm{E}}(Q^2)$ for the halo nuclei ^{11}Li (left plot, blue solid line), ^{12}Be (left plot, red long-dashed line) and ^{22}C (right plot, green dash dotted line) relative to the core in leading order halo EFT. The estimated theory error for ^{11}Li and ^{12}Be is given by the shaded bands. For ^{22}C, varying the separation energies within their errors gives the shaded region. The vertical dashed lines indicate the breakdown scale from explicit pion exchange.

threshold. The first excitation energy of the ^{9}Li ground state is 2.69 MeV and its one-neutron separation energy is 4.06 MeV. Thus the expansion parameter and the error can be estimated as $R_{\mathrm{core}}/R_{\mathrm{halo}} \approx \sqrt{B_{cnn}/E_c^*} \approx 0.37$. Calculating the charge radius relative to ^{9}Li via Eq. (32) gives $\delta \langle r_{\mathrm{E}}^2 \rangle = 1.68(62)$ fm^2, where the $\sim 40\%$ uncertainty comes from the expansion parameter. In Ref. [29], the charge radius was measured with the help of high precision laser spectroscopy. The experimental value of $\delta \langle r_{\mathrm{E}}^2 \rangle_{\mathrm{exp}} = 1.171(120)$ fm^2 is thus compatible with our calculation within the error bars.

The halo nucleus ^{14}Be and its core ^{12}Be are both in a $J^\pi = 0^+$ configuration, while the quantum numbers of ^{13}Be are less clear although there is some evidence for $J^\pi = \frac{1}{2}^-$. For our study, we assume that the ^{13}Be dimer has also positive parity. The binding energy of the ^{14}Be trimer is $B_{cnn} = 1.27(13)$ MeV and the virtual ^{13}Be has $B_{cn} = -510(10)$ keV. The excitation energy of the ^{10}Be core is $E_c^* = 2.10$ MeV and its one-neutron separation energy is 3.17 MeV. Thus, the resulting expansion parameter $R_{\mathrm{core}}/R_{\mathrm{halo}} \approx \sqrt{B_{cnn}/E_c^*} \approx 0.78$ is relatively large. Using Eq. (32), our effective theory then predicts a charge radius relative to ^{12}Be of $\delta \langle r_{\mathrm{E}}^2 \rangle = 0.41(32)$ fm^2 with an $\sim 80\%$ error.

There is some theoretical and experimental evidence that ^{22}C is a pure S-wave halo nucleus [36, 37]. ^{22}C and the ^{20}C core both have $J^\pi = 0^+$, while ^{21}C is in $J^\pi = \frac{1}{2}^+$ configuration. The two-neutron separation energy $B_{cnn} = 0.11(6)$ MeV has a relatively large error. Furthermore, ^{21}C seems to be unbound, but $B_{cn} = -0.014(467)$ keV is only poorly known. Up to now, no excitations of the core were observed. The one-neutron separation energy of ^{20}C is 2.9(3) MeV. We take the central values for B_{cnn} and B_{cn}, which are also roughly in accord with the allowed parameter region predicted from a recent analysis of the matter radius measurement [37] in the framework of the halo EFT [38]. Calculating the charge radius relative to ^{20}C via Eq. (32) gives $\delta \langle r_\mathrm{E}^2 \rangle = 1.66^{+\infty}_{-0.49}$ fm^2, where the uncertainty now comes from varying the separation energies within their errors. Due to the poorly known input data, $B_{cn} = B_{cnn}$ is not excluded. Since for such values, the charge radius diverges towards positive infinity, the predicted value for $\delta \langle r_\mathrm{E}^2 \rangle$ can only be bound from below, where the lower limit is 1.17 fm^2. For the halo nuclei ^{14}Be and ^{22}C, our results are true predictions and can be compared with measurements as soon as the corresponding experimental data is available.

In Fig. 7, the charge form factors calculated from Eq. (30) are depicted as a function of the momentum transfer Q^2. For $Q^2 \to \infty$, the form factors vanish. At small momentum transfers, they approach unity as required by current conservation. Numerical deviations from unity at vanishing Q^2 are less than 10^{-5}. This provides a consistency-check for our calculation. For ^{11}Li and ^{12}Be, the estimated error from higher orders in the effective theory expansion is given by the shaded bands. For ^{22}C the shaded region originates from varying the binding energies within their errors. Our effective theory does neither include explicit pion dynamics nor does it include the structure of the core. Thus it breaks breaks down for momentum transfers of the order of the pion mass $m_\pi^2 \approx 0.5$ fm^{-2} as indicated by the vertical dashed lines in Fig. 7.

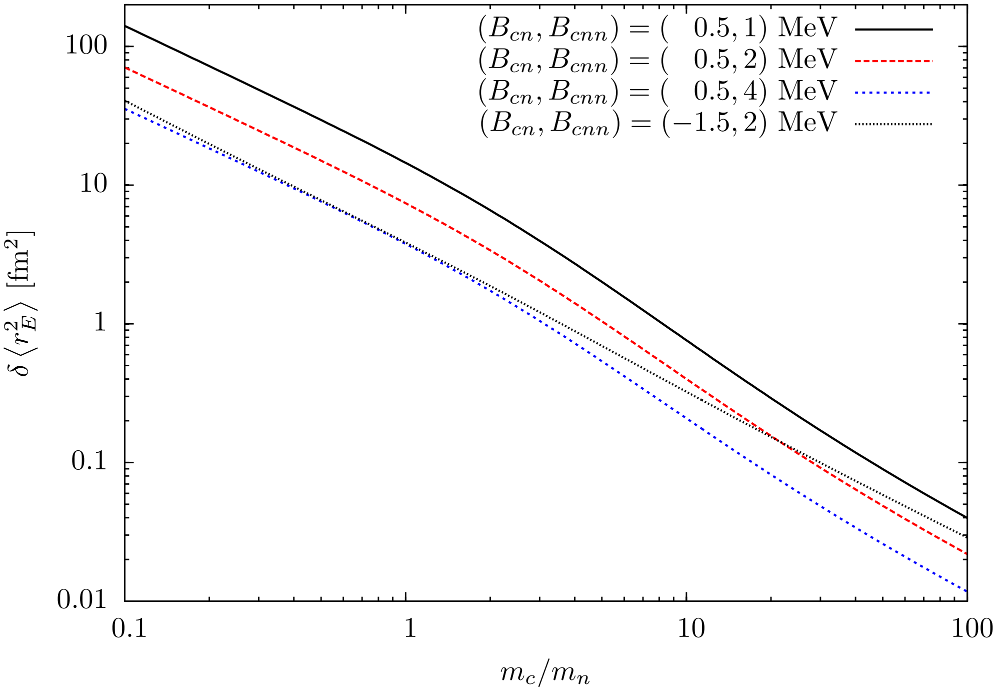

FIG. 8: (Color online) The electric charge radius relative to the core $\delta \langle r_\mathrm{E}^2 \rangle$ as a function of mass ratio m_c/m_n for different binding energies B_{cn} and B_{cnn}.

Another interesting aspect is to understand the general dependencies of the charge radius on the core mass and the cn and cnn binding energies. In Fig. 8, we therefore plot $\delta \langle r_\mathrm{E}^2 \rangle$ as a function of the mass ratio m_c/m_n for fixed energy values B_{cnn} and B_{cn}. The charge

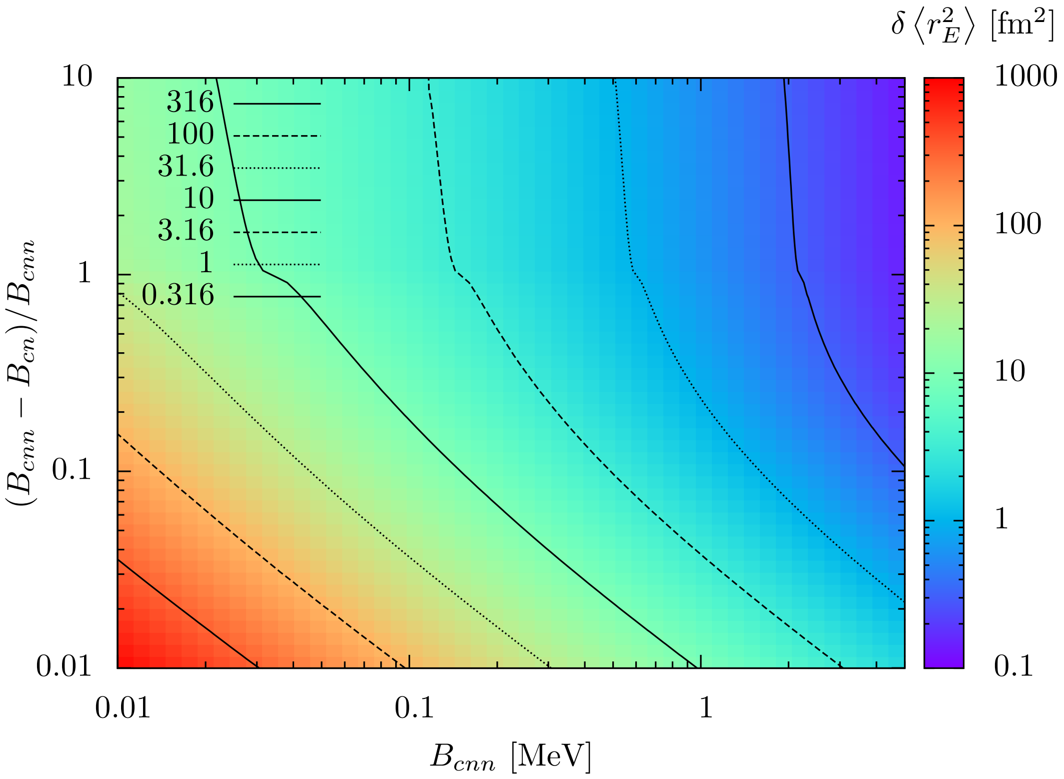

FIG. 9: (Color online) The electric charge radius relative to the core $\delta \langle r_{\mathrm{E}}^2 \rangle$ as a function of the energies B_{cnn} and $1 - B_{cn}/B_{cnn}$ for fixed mass ratio $m_c/m_n = 10$.

radius is always positive and decreases for growing core mass m_c. This reflects that $\delta \langle r_{\mathrm{E}}^2 \rangle$ for the two-neutron halo system originates from the recoil effect of the charged core. For core masses below $2m_n$ the radius roughly falls of like $\sim 1/m_c$. Around $m_c \approx 2m_n$, the slope changes and the charge radii drop even faster as m_c/m_n increases.

In Fig. 9, the dependence of the charge radius relative to the core on the energies B_{cnn} and $1 - B_{cn}/B_{cnn}$ is shown for a fixed mass ratio $m_c/m_n = 10$. As one would also naively expect, $\delta \langle r_{\mathrm{E}}^2 \rangle$ grows as both the binding energies for the three-body system B_{cnn} and the binding energy of the dimer-particle system $B_{cnn} - B_{cn}$ decrease. However, the exact functional dependencies on the 3 quantities m_c, B_{cnn} and B_{cn} are more complicated. Also note that there is a sudden increase in $\delta \langle r_{\mathrm{E}}^2 \rangle$ along the line $B_{cn} = 0$ where the cn-system changes from a bound state to a virtual state. This leads to a ridge along $(B_{cnn} - B_{cn})/B_{cnn} = 1$ that is most easily seen in the contour lines.

VIII. SUMMARY AND CONCLUSION

In this paper, we have set up a formalism to describe the electromagnetic structure of $2n$ halo nuclei within halo EFT. We assumed that the cn and nn S-wave scattering lengths are much larger than the range of the interaction and calculated the form factors and charge radii of various halo nuclei to leading order in the expansion in $R_{\text{core}}/R_{\text{halo}}$. The renormalization of the trimer propagator and the extraction of the trimer wave function renormalization were discussed in detail. The charge form factor receives contributions from three different classes of diagrams illustrated in Fig. 6. In all three contributions, the irreducible trimer-dimer-particle three-point function $\vec{\mathcal{G}}^{\mathrm{irr}}$ from Eq. (26) appears naturally. Current conservation insures the correct normalization of the charge form factor $\mathcal{F}_{\mathrm{E}}(0) = 1$. Numerically, we find deviations from unity at vanishing Q^2 of less than 10^{-5} in our calculation.

We have applied our formalism to ^{11}Li, ^{14}Be and ^{22}C calculated their charge form factors and radii relative to the core to leading order in $R_{\mathrm{core}}/R_{\mathrm{halo}}$. The resulting charge radii are $\delta\,\langle r_{\mathrm{E}}^2\rangle_{^{11}\mathrm{Li}} = 1.68(62)$ fm^2, $\delta\,\langle r_{\mathrm{E}}^2\rangle_{^{14}\mathrm{Be}} = 0.41(32)$ fm^2, and $\delta\,\langle r_{\mathrm{E}}^2\rangle_{^{22}\mathrm{C}} = 1.66^{+\infty}_{-0.49}$ fm^2. For ^{11}Li a comparison with the measured value 1.171(120) fm^2 shows good agreement within the $\sim 40\%$ uncertainty originating from the expansion parameter of our leading order calculation. The other charge radii are true predictions that can be compared to future experiments. For a more quantitative comparison with experiment, the extension to higher orders is clearly required. This includes the treatment of effective range effects [23–25] as well as of P-wave interactions in ^{11}Li and ^{14}Be. Electromagnetic breakup reactions can reveal additional information on the structure of $2n$ halo nuclei. An investigation of this process in the framework of halo EFT is in progress [39].

Finally, we have investigated the dependence of the charge radius on the core mass and the cnn and cn binding energies. Our results are summarized in Figs. 8 and 9. As expected, the charge radius decreases with increasing core radius. However, the exact dependence for for large core masses deviates from a simple $1/m_c$ dependence. Moreover, the charge radius increases as binding energies $B_{cnn} - B_{cn}$ and B_{cnn} decrease. In particular, we found a sudden increase of the charge radius along the line $B_{cn} = 0$ where the cn-system changes from a bound state to a virtual state. A better understanding of these characteristics will require further studies.

Acknowledgments

We thank D.R. Phillips for discussions. This work was supported in part by the DFG and the NSFC through funds provided to the Sino-German CRC 110 “Symmetries and the emergence of structure in QCD”, by the BMBF under contract 06BN7008, and by the US Department of Energy, Office of Nuclear Physics, under Contract No. DE-AC02-06CH11357.

Appendix A: Form factor contributions

In this appendix, we explicitly derive the three different contributions to the charge form factor discussed in Sec. VI. Therefore, we first give an expression for $i\Gamma_0(\mathbf{Q})$ from Eq. (29) as the sum of all irreducible Feynman diagrams with external trimer lines and a photon coupled to the core. It can be conveniently written as

$$\begin{aligned} i\Gamma_0(\mathbf{Q}) &= \int\limits_{|\mathbf{p}|<\Lambda} \frac{\mathrm{d}^4 p}{(2\pi)^4} \int\limits_{|\mathbf{k}|<\Lambda} \frac{\mathrm{d}^4 k}{(2\pi)^4} \\ &\quad \times\ i\vec{\mathcal{G}}^{\mathrm{irr}}(E,\mathbf{P},p_0,\mathbf{p})^{\mathrm{T}}\ i\bar{\Gamma}_0(E,\mathbf{P},p_0,\mathbf{p},\mathbf{K},k_0,\mathbf{k})\ i\vec{\mathcal{G}}^{\mathrm{irr}}(E,\mathbf{K},k_0,\mathbf{k})\ . \end{aligned} \tag{A1}$$

The quantity $\mathcal{G}_i^{\mathrm{irr}}(E,\mathbf{P},p_0,\mathbf{p})$ is the irreducible trimer-dimer-particle three-point function in general kinematics, where the trimer, dimer and particle four-momenta are written as P^μ, $\frac{M_i}{M_{\mathrm{tot}}}P^\mu + p^\mu$ and $\frac{m_i}{M_{\mathrm{tot}}}P^\mu - p^\mu$, respectively. The energy reads $E = P_0 - \mathbf{P}^2/(2M_{\mathrm{tot}})$, where the kinetic energy of the three-body bound state is subtracted. $\mathcal{G}_i^{\rm irr}(E,\mathbf{P},p_0,\mathbf{p})$ is related to the center-of-mass quantity $\mathcal{G}_i^{\rm irr}(E,p)$ from Eq. (26) through the integral equation

$$\begin{aligned}\mathcal{G}_i^{\rm irr}(E,\mathbf{P},p_0,\mathbf{p}) \;=\; &\sum_{j=0}^{1}\int_0^\Lambda \mathrm{d}q\; R_{ij}\Big(\frac{M_i}{M_{\rm tot}}E + p_0 - \frac{\mathbf{P}\cdot\mathbf{p}}{M_{\rm tot}} + \frac{\mathbf{p}^2}{2m_i}, p, q\Big)\Big|_{H=0} \\ &\times\; \bar{D}_j(E,q)\,\mathcal{G}_j^{\rm irr}(E,q) \;+\; \delta_{0i}\;.\end{aligned} \tag{A2}$$

The matrix valued function $i\bar{\Gamma}_0$ in Eq. (A1) is the sum of the three diagrams that are depicted in the lower row in Fig. 6. Its contributions (a), (b), and (c) are products of the corresponding delta-functions, propagators and couplings.

Since in the Breit frame in- and outgoing three-body bound states have $E = -B$, we drop this redundant energy variable in $\vec{\mathcal{G}}^{\rm irr}$ and $\bar{D}$ in all subsequent equations.

1. Contribution $\mathcal{F}^{(a)}$

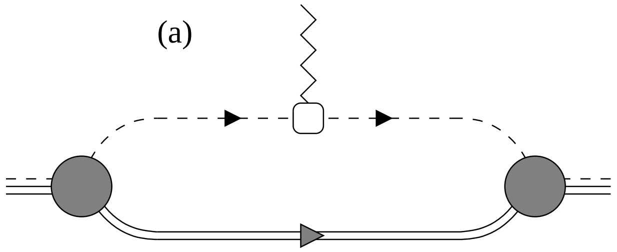

FIG. 10: Type-(a) contribution to the form factor matrix element where the photon couples to a core field propagating parallel to the d_0-dimer. Notation is as in Fig. 4.

We start with the type-(a) contribution depicted in Fig. 10 where the photon couples to a core field propagating parallel to a d_0-dimer. All non-perturbative physics is contained in the irreducible trimer-dimer-particle three-point function $\vec{\mathcal{G}}^{\rm irr}$. One of the two four-momentum integrations in Eq. (A1) is absorbed by a delta-function and the remaining loop four-momentum q^μ can be chosen in such a way that the resulting expression is symmetric under $\mathbf{q} \mapsto -\mathbf{q}$. The q^0 integration can then be performed analytically, leading to two contributions from picking the poles of the two core propagators. The trimer-dimer-particle three-point functions $\mathcal{G}^{\rm irr}$ appear in off-shell kinematics and are related to on-shell center-of-mass quantities via Eq. (A2) at the expense of two additional momentum integrations. Choosing spherical coordinates for $\mathbf{q}$, with $\mathbf{Q} = \mathbf{K} - \mathbf{P}$ pointing in the z-direction, the azimuthal dependence can also be integrated out. We are then left with a remaining integral over $q = |\mathbf{q}|$ and the polar angle $x = \cos(\angle(\mathbf{Q},\mathbf{q}))$. Since the d_0 dimer is propagating parallel to the core, the integral equation (27) leads to extra contributions from the three-body force. Finally, we end up with

$$\begin{aligned}\mathcal{F}^{(a)}(Q^2) \;=\; Z_{\rm tr}\,H^2\Bigg\{&\int_0^\Lambda \mathrm{d}p \int_0^\Lambda \mathrm{d}k\; \vec{\mathcal{G}}^{\rm irr}(p)^{\rm T}\,\bar{D}(p)\;\Upsilon^{(a)}(Q,p,k)\;\bar{D}(k)\,\vec{\mathcal{G}}^{\rm irr}(p) \\ &+\;2\int_0^\Lambda \mathrm{d}p\,\vec{\mathcal{G}}^{\rm irr}(p)^{\rm T}\,\bar{D}(p)\;\vec{\Upsilon}^{(a)}(Q,p)\;+\;\Upsilon_0^{(a)}(Q)\Bigg\}\;,\end{aligned} \tag{A3}$$

where the matrix-, vector- and scalar-valued functions $\Upsilon^{(a)}(Q,p,k)$, $\vec{\Upsilon}^{(a)}(Q,p)$ and $\Upsilon_0^{(a)}(Q)$, using the shortened notation $\Upsilon^{(a)}_{\dots}(Q\dots)$, are given by:

$$\Upsilon^{(a)}_{\dots}(Q\dots) \;=\; \frac{\tilde{\mu}_0}{4}\int_0^{\Lambda}\frac{\mathrm{d}q}{q}\int_{-1}^{1}\frac{\mathrm{d}x}{x}\,\chi^{(a)}_{\dots}\left(\frac{M_0}{M_{\mathrm{tot}}}\frac{Q}{2},q,x\dots\right)\;, \tag{A4}$$

where

$$\begin{aligned}
\chi^{(a)}_{ij}(r,q,x,p,k) \;&=\frac{1}{r}\Bigg\{R_{i0}\Big(-B+2\frac{qrx}{\tilde{\mu}_0},p,d(r,q,x)\Big)\Big|_{H=0}\,\bar{D}_0\left(-B-\frac{m_0\,r^2}{2\tilde{\mu}_0^2}+\frac{qrx}{\tilde{\mu}_0},q\right)\\
&\qquad\times\;R_{0j}(-B,d(r,q,-x),k)\Big|_{H=0}\\
&\quad-\;R_{i0}(-B,p,d(r,q,x))\Big|_{H=0}\,\bar{D}_0\left(-B-\frac{m_0\,r^2}{2\tilde{\mu}_0^2}-\frac{qrx}{\tilde{\mu}_0},q\right)\\
&\qquad\times\;R_{0j}\Big(-B-2\frac{qrx}{\tilde{\mu}_0},d(r,q,-x),k\Big)\Big|_{H=0}\Bigg\}\;,\\
\chi^{(a)}_{i}(r,q,x,p) \;&=\frac{1}{r}\Bigg\{R_{i0}\Big(-B+2\frac{qrx}{\tilde{\mu}_0},p,d(r,q,x)\Big)\Big|_{H=0}\,\bar{D}_0\left(-B-\frac{m_0\,r^2}{2\tilde{\mu}_0^2}+\frac{qrx}{\tilde{\mu}_0},q\right)\\
&\quad-R_{i0}(-B,p,d(r,q,x))\Big|_{H=0}\,\bar{D}_0\left(-B-\frac{m_0\,r^2}{2\tilde{\mu}_0^2}-\frac{qrx}{\tilde{\mu}_0},q\right)\Bigg\}\;,\\
\chi^{(a)}_{0}(r,q,x) \;&=\frac{1}{r}\Bigg\{\bar{D}_0\left(-B-\frac{m_0\,r^2}{2\tilde{\mu}_0^2}+\frac{qrx}{\tilde{\mu}_0},q\right)\;-\;\bar{D}_0\left(-B-\frac{m_0\,r^2}{2\tilde{\mu}_0^2}-\frac{qrx}{\tilde{\mu}_0},q\right)\Bigg\}\;,
\end{aligned} \tag{A5}$$

with $d(r,q,x)=\sqrt{q^2+2qrx+r^2}$. One can easily check that the symmetry $\Upsilon^{(a)}(Q,p,k)=\Upsilon^{(a)}(Q,k,p)^{\mathrm{T}}$ holds as required. Note also that the limit $Q\to 0$ in Eq. (A5) exists, but prefactors $\propto 1/Q$ cause numerical instabilities for very small momentum transfer.

2. Contribution $\mathcal{F}^{(b)}$

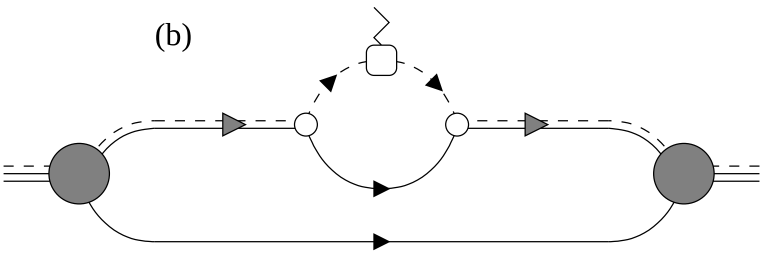

FIG. 11: Type-(b) contribution to the form factor matrix element where the photon couples to a core field inside a *nc* bubble. Notation is as in Fig. 4.

We now consider contributions to the formfactor of type (b), where the photon couples to a core field inside a *nc* bubble. The corresponding Feynman diagram is depicted in Fig. 11.

The bubble sub-diagram can be calculated analytically using Feynman integrals. Analogue to case (a) one of the two four-momentum integrations in Eq. (A1) is absorbed by a delta-function and the remaining loop four-momentum q^μ can be chosen in a symmetric way. Applying Eq. (A2) then again leads to two additional momentum integrations. In spherical coordinates, the azimuthal integration can then be performed leading to two remaining integrals over $q = |\mathbf{q}|$ and the polar angle $x = \cos(\angle(\mathbf{Q}, \mathbf{q}))$. Since diagrams of type (b) only appear in channel 1 where the neutron-core dimer is present, there are no three-body force contributions in the integral. We find

$$\mathcal{F}^{(b)}(Q^2) \;=\; Z_{\mathrm{tr}}\, H^2 \int_0^\Lambda \mathrm{d}p \int_0^\Lambda \mathrm{d}k\; \vec{\mathcal{G}}^{\mathrm{irr}}(p)^{\mathrm{T}}\; \bar{D}(p)\; \Upsilon^{(b)}(Q,p,k)\; \bar{D}(k)\; \vec{\mathcal{G}}^{\mathrm{irr}}(k)\;, \tag{A6}$$

where the matrix-valued function $\Upsilon^{(b)}(Q,p,k)$ is given through:

$$\begin{aligned}
\Upsilon^{(b)}_{ij}(Q,p,k) \;&=\; \frac{\mu_1\,|a_1|}{(2\pi)^2}\,\frac{m_0 m_1}{2M_{\mathrm{tot}}} \int_0^\Lambda \mathrm{d}q\, q^2 \int_{-1}^{1} \mathrm{d}x\; \chi^{(b)}_{ij}\left(\frac{m_1}{M_{\mathrm{tot}}}\frac{Q}{2}, q, x, p, k\right)\;,\\
\chi^{(b)}_{ij}(s,q,x,p,k) \;&=\; \frac{R_{i1}(-B,p,d(s,q,-x))\Big|_{H=0}}{\frac{1}{a_1} - \sqrt{b_1(-B,d(s,q,-x))}}\;\frac{1}{s}\left\{\arctan\left(\frac{\frac{M_{\mathrm{tot}}}{M_1}s + \frac{m_0}{M_1}qx}{\sqrt{b_1(-B,d(s,q,-x))}}\right)\right.\\
&\quad\left. +\;\arctan\left(\frac{\frac{M_{\mathrm{tot}}}{M_1}s - \frac{m_0}{M_1}qx}{\sqrt{b_1(-B,d(s,q,x))}}\right)\right\}\;\frac{R_{1j}(-B,d(s,q,x),k)\Big|_{H=0}}{-\frac{1}{a_1} + \sqrt{b_1(-B,d(s,q,x))}}\;.
\end{aligned} \tag{A7}$$

Again $\Upsilon^{(b)}(Q,p,k) = \Upsilon^{(b)}(Q,k,p)^{\mathrm{T}}$ holds and the limit $Q \to 0$ can lead to numerical instabilities.

3. Contribution $\mathcal{F}^{(c)}$

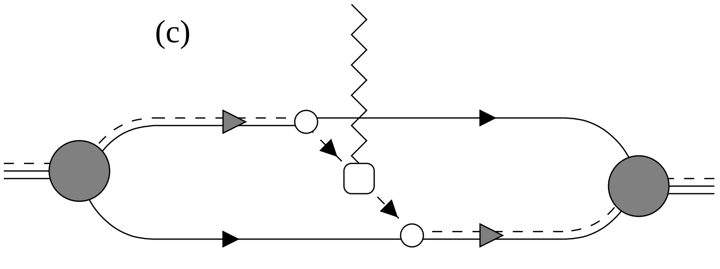

FIG. 12: Type-(c) contribution to the form factor matrix element where the photon couples to a core field exchanged between $\vec{d}_1$ dimers. Notation is as in Fig. 4.

In the remaining contribution of type (c) shown in Fig. 12, the photon couples to a core field that is exchanged between $\vec{d}_1$ dimers. For both loops, the energy integrals can be performed analytically, leading to on-shell conditions for the trimer-dimer-particle three-point function $\mathcal{G}^{\mathrm{irr}}$. In spherical coordinates, one of the two azimuthal integrals can be solved analytically, such that in the end five integrals remain. For $\mathcal{F}^{(c)}$, we then get

$$\mathcal{F}^{(c)}(Q^2) \;=\; Z_{\mathrm{tr}}\, H^2 \int_0^\Lambda \mathrm{d}p \int_0^\Lambda \mathrm{d}k\; \vec{\mathcal{G}}^{\mathrm{irr}}(p)^{\mathrm{T}}\; \bar{D}(p)\; \Upsilon^{(c)}(Q,p,k)\; \bar{D}(k)\; \vec{\mathcal{G}}^{\mathrm{irr}}(k)\;, \tag{A8}$$

with a the matrix-valued function $\Upsilon^{(c)}(Q,p,k)$ given by:

$$\begin{aligned}
\Upsilon^{(c)}_{ij}(Q,p,k) &= \frac{2}{|a_1|}\int_{-1}^{1}\mathrm{d}x\int_{-1}^{1}\mathrm{d}y\int_{0}^{\pi}\mathrm{d}\phi\;\chi^{(c)}_{ij}\left(\frac{m_1}{M_{\mathrm{tot}}}Q,x,y,\phi,p,k\right)\;,\\
\chi^{(c)}_{ij}(t,x,y,\phi,p,k) &= \delta_{i1}\,\delta_{1j}\\
\times&\left[p^2+k^2+t^2-2\left(ky+\frac{m_1}{M_1}px\right)t+2\frac{m_1}{M_1}pk\left[\sqrt{1-x^2}\sqrt{1-y^2}\cos\phi+xy\right]+2\mu_1 B\right]^{-1}\\
\times&\left[p^2+k^2+t^2+2\left(px+\frac{m_1}{M_1}ky\right)t+2p\frac{m_1}{M_1}k\left[\sqrt{1-x^2}\sqrt{1-y^2}\cos\phi+xy\right]+2\mu_1 B\right]^{-1}
\end{aligned}\tag{A9}$$

As in the other cases, the symmetry condition $\Upsilon^{(c)}(Q,p,k)=\Upsilon^{(c)}(Q,k,p)^{\mathrm{T}}$ holds.

The dependence of all three formfactor contributions (a), (b), and (c) on Q^2 only is not directly evident from Eqs. (A3), (A6) and (A8) but numerically it is satisfied. Moreover, the charge form factor $\mathcal{F}(Q^2)$ is automatically normalized to unity at zero momentum transfer.

[1] K. Riisager, Rev. Mod. Phys. **66**, 1105 (1994).

[2] M.V. Zhukov, B.V. Danilin, D.V. Fedorov, J.M. Bang, I.J. Thompson, and J.S. Vaagen, Phys. Rep. **231**, 151 (1993).

[3] P.G. Hansen, A.S. Jensen, and B. Jonson, Ann. Rev. Nucl. Part. Sci. **45**, 591 (1995).

[4] A.S. Jensen, K. Riisager, D.V. Fedorov, and E. Garrido, Rev. Mod. Phys. **76**, 215 (2004).

[5] C.A. Bertulani, H.-W. Hammer and U. Van Kolck, Nucl. Phys. A **712**, 37 (2002) [arXiv:nucl-th/0205063].

[6] P.F. Bedaque, H.-W. Hammer and U. van Kolck, Phys. Lett. B **569**, 159 (2003) [arXiv:nucl-th/0304007].

[7] L. Platter, Few-Body Syst. **46**, 139 (2009) [arXiv:0904.2227].

[8] H.-W. Hammer and L. Platter, Ann. Rev. Nucl. Part. Sci. **60**, 207 (2010) [arXiv:1001.1981 [nucl-th]].

[9] D. L. Canham and H.-W. Hammer, Eur. Phys. J. A **37**, 367 (2008) [arXiv:0807.3258 [nucl-th]].

[10] D. L. Canham and H.-W. Hammer, Nucl. Phys. A **836**, 275 (2010) [arXiv:0911.3238 [nucl-th]].

[11] V. Efimov, Phys. Lett. **33B**, 563 (1970).

[12] B. Acharya, C. Ji and D. R. Phillips, [arXiv:1303.6720 [nucl-th]].

[13] D.V. Fedorov, A.S. Jensen and K. Riisager, Phys. Rev. Lett. **73**, 2817 (1994) [arXiv:nucl-th/9409018].

[14] A.E.A. Amorim, T. Frederico and L. Tomio, Phys. Rev. C **56**, R2378 (1997) [arXiv:nucl-th/9708023].

[15] I. Mazumdar, V. Arora and V. S. Bhasin, Phys. Rev. C **61**, R051303 (2000).

[16] M. T. Yamashita, L. Tomio and T. Frederico, Nucl. Phys. A **735**, 40 (2004) [arXiv:nucl-th/0401063].

[17] R. Higa, H.-W. Hammer and U. van Kolck, Nucl. Phys. A **809**, 171 (2008) [arXiv:0802.3426 [nucl-th]].

[18] H.-W. Hammer and D. R. Phillips, Nucl. Phys. A **865**, 17 (2011) [arXiv:1103.1087 [nucl-th]].

[19] G. Rupak and R. Higa, Phys. Rev. Lett. **106**, 222501 (2011) [arXiv:1101.0207 [nucl-th]].
[20] G. Rupak, L. Fernando, and A. Vaghani, Phys. Rev. C **86**, 044608 (2012) [arXiv:1204.4408 [nucl-th]].
[21] B. Acharya and D. R. Phillips, [arXiv:1302.4762 [nucl-th]].
[22] P. F. Bedaque, G. Rupak, H. W. Grießhammer and H.-W. Hammer, Nucl. Phys. A **714**, 589 (2003) [nucl-th/0207034].
[23] D. B. Kaplan, Nucl. Phys. B **494**, 471 (1997) [nucl-th/9610052].
[24] H.-W. Hammer and T. Mehen, Phys. Lett. B **516**, 353 (2001) [nucl-th/0105072].
[25] C. Ji, D. R. Phillips and L. Platter, Annals Phys. **327**, 1803 (2012) [arXiv:1106.3837 [nucl-th]].
[26] G.V. Skorniakov and K.A. Ter-Martirosian, Sov. Phys. JETP **4**, 648 (1957).
[27] D. B. Kaplan, M. J. Savage and M. B. Wise, Phys. Rev. C **59**, 617 (1999) [nucl-th/9804032].
[28] S. Kopecky, M. Krenn, P. Riehs, S. Steiner, J. A. Harvey, N. W. Hill and M. Pernicka, Phys. Rev. C **56**, 2229 (1997).
[29] R. Sánchez et al., Phys. Rev. Lett. **96**, 033002 (2006) [arXiv:physics/0509265].
[30] W. Nörtershäuser et al., Phys. Rev. Lett. **102**, 062503 (2009) [arXiv:0809.2607].
[31] A. Krieger et al., Phys. Rev. Lett. **108**, 142501 (2012) [arXiv:1202.4873].
[32] W. Geithner et al., Phys. Rev. Lett. **101**, 252502 (2008).
[33] D.T. Yordanov et al., Phys. Rev. Lett. **108**, 042504 (2012).
[34] D.E. Gonzáles Trotter et al., Phys. Rev. Lett. **83**, 3788 (1999) [arXiv:nucl-ex/9904011].
[35] Chart of Nuclides, National Nuclear Data Center, Brookhaven National Laboratory [http://www.nndc.bnl.gov/chart/].
[36] W. Horiuchi and Y. Suzuki, Phys. Rev. C **74**, 034311 (2006) [arXiv:nucl-th/0605055].
[37] K. Tanaka et al., Phys. Rev. Lett. **104**, 062701 (2010).
[38] B. Acharya, C. Ji, and D. R. Phillips, [arXiv:1303.6720 [nucl-th]].
[39] B. Acharya, P. Hagen, H.-W. Hammer and D. R. Phillips, work in progress.